Experimental investigation of a non-Abelian gauge field in 2D perovskite photonic platform

L Polimeno, A Fieramosca, G Lerario, L de Marco, M de Giogi, D Ballarini, L Dominici, V Ardizzone, M Pugliese, C Prontera, et al.

OPTICA

Experimental investigation of a non-Abelian gauge field in 2D perovskite photonic platform

L. Polimeno,[1,2,†] A. Fieramosca,[1,2,†] G. Lerario,[1,5] L. De Marco,[1,6] M. De Giorgi,[1] D. Ballarini,[1] L. Dominici,[1] V. Ardizzone,[1] M. Pugliese,[1] C. T. Prontera,[1] V. Maiorano,[1] G. Gigli,[1,2] C. Leblanc,[3] G. Malpuech,[3,7] D. D. Solnyshkov,[3,4,8] and D. Sanvitto[1]

[1]CNR Nanotec, Institute of Nanotechnology, via Monteroni, 73100, Lecce, Italy
[2]Dipartimento di Matematica e Fisica, "Ennio de Giorgi", Universitá del Salento, via Arnesano, 73100 Lecce, Italy
[3]Institut Pascal, PHOTON-N2, Université Clermont Auvergne, CNRS, SIGMA Clermont, F-63000 Clermont-Ferrand, France
[4]Institut Universitaire de France (IUF), 75231 Paris, France
[5]e-mail: giovannilerario86@gmail.com
[6]e-mail: luisademarco@nanotec.cnr.it
[7]e-mail: malpuech@lasmea.univ-bpclermont.fr
[8]e-mail: dmitry.solnyshkov@univ-bpclermont.fr

Received 6 April 2021; revised 27 May 2021; accepted 7 June 2021 (Doc. ID 427088); published 9 November 2021

Electromagnetism, with its scalar charges, is based on an Abelian gauge theory, whereas non-Abelian gauge theories with vector charges describe strong and weak interactions, with a coupled spatial and charge (color) dynamics. New Abelian gauge fields have been synthesized artificially, allowing the study of extraordinary physical effects. The most well-known example is the Berry curvature, the cornerstone of topological physics. Synthetic non-Abelian gauge fields have been implemented only recently, but their action on the spatial dynamics of their emergent charges has not been studied experimentally so far. Here, by exploiting optically anisotropic 2D perovskite in the strong light–matter coupling regime, we experimentally synthesized a static non-Abelian gauge field, acting on an exciton-polariton quantum flow at room temperature. We observe experimentally the corresponding curved trajectories and spin precession. Our work could therefore open perspectives to study the non-Abelian physics using highly flexible photonic simulators.

https://doi.org/10.1364/OPTICA.427088

1. INTRODUCTION

Historically, the first gauge theory was developed for the electromagnetic field in 1865. It is an Abelian gauge theory: the particle charges are scalars and the components of the vector potential commute with each other. The next step was realized by Yang and Mills [1] who introduced a non-Abelian gauge theory by replacing a scalar charge by a vector, i.e., the isospin. The components of the vector potential are the Pauli matrices forming the SU(2) group, which do not commute [2]. Complemented by the Higgs mechanism [3], non-Abelian Yang–Mills gauge theories for both the strong and the weak interactions allow to build the whole standard model of elementary particles [4].

Since then, a new playground has been found for gauge theories with the invention and experimental implementation of emergent gauge fields [5]. The most well-known example is the Berry curvature, which is often interpreted as a magnetic field analog [6], but defined in a parameter space (e.g., momentum space). In all cases, the evolution along a trajectory—either in parameter or real space—is associated with an additional phase (Berry or Aharonov–Bohm phase). Topological physics can therefore be considered a consequence of an emergent Abelian gauge field, similar to the electromagnetic field [7–10]. Real-space Abelian gauge fields are already successfully used in photonics for spin filtering [11]. In contrast, emergent *non-Abelian* gauge fields have been much less explored so far.

A promising strategy relies on recently discovered mapping [12,13] between the Rashba spin-orbit coupling (SOC) [14] for massive particles, well-known in solid state physics, and the static limit of a non-Abelian gauge field of the Yang–Mills type. This mapping opened the exciting perspective of developing analogue non-Abelian gauge field theories in solid state systems.

It is crucial to distinguish recent different realizations of artificial Rashba-like SOCs. Alone, or with a "mass"-like term, it gives a 2D Dirac Hamiltonian with non-commuting x and y projections, but without a non-Abelian gauge field (see Supplement 1, Section III). A 1D Dirac Hamiltonian has been first implemented in cold atoms systems [15], followed by a 2D realization [16]. Only when the Rashba SOC applies in addition to the main kinetic energy term for a particle described by the Schrödinger equation, it can be considered as a minimally coupled non-Abelian gauge potential. A scheme to synthesize such Rashba (and similar) SOC has been theoretically proposed for photons [17,18] and only very

recently implemented experimentally using planar microcavities in the strong exciton–photon coupling regime [19] and filled with liquid crystals [20]. At the same time, other researchers confronted the problem of non-Abelian gauge fields from another side, by considering a non-Abelian version of the Aharonov–Bohm effect [21,22]. It consists of making the light polarization pseudospin successively rotate across two differently oriented effective magnetic fields. Indeed, the final pseudospin orientation depends on the ordering of the two constant fields. This ordering sensitivity is a consequence of the non-commutativity of Pauli matrices. However, the corresponding terms are the *time-like* components of the four-vector potential, affecting the phase and the interference of the particles, but not their real space trajectories.

In this work, we implement experimentally another type of non-Abelian vector potential with *space-like* components, affecting the real space trajectories via an analog of the Lorentz force. This vector potential is deduced from the mapping to a Rashba–Dresselhaus bosonic Hamiltonian, which emerges from a 2D confined optical system with both linear birefringence and energy splitting between TE (transverse electric) and TM (transverse magnetic) polarized modes. The non-Abelian character of the gauge field implies the existence of a non-zero effective magnetic field. In the following, we provide a direct measurement of the transverse acceleration of an exciton-polariton wave packet, caused by the resulting effective magneto-static force, together with the corresponding spin precession. This coupled spatial and spin dynamics is successfully described by analytical equations of motion. We therefore have an SU(2) non-Abelian gauge field with a direct experimental accessibility.

2. RESULTS

The sample is based on a single crystal of 2D hybrid organic–inorganic perovskite (Fig. 1A) placed in an asymmetric planar microcavity (Fig. 1B). The active material is 4-fluorophenethylammonium tetraiodoplumbate (henceforth referred to as PEAI-F), a multiple quantum well system consisting of $(PbI_6)^{4-}$ layers sandwiched between organic insulator layers. The quality factor of the planar microcavity modes is $Q_f \simeq 1000$. The wavevector k_z of the bare light modes perpendicular to the mirrors is quantized, giving rise to a series of 2D bands, with approximately parabolic dispersion at k_x, $k_y \sim 0$. The role of the *charge vector* in our case is played by the pseudospin associated with the polarization of light. The components of the pseudospin, which in our case is the Stokes vector of light, are directly determined by the polarization degrees, measured in three possible bases: horizontal/vertical (HV, s^1), diagonal/antidiagonal (DA s^2), and left/right circular (LR, s^3). The explicit expressions allowing to obtain the pseudospin from the measured intensities read

$$s^1 = \frac{I_V - I_H}{I_V + I_H},$$

$$s^2 = \frac{I_D - I_A}{I_D + I_A},$$

$$s^3 = \frac{I_R - I_L}{I_R + I_L}. \quad (1)$$

The spin-orbit coupling arises from the energy splitting between the microcavity TE and TM modes[17]. The polarized modes form two parabola with different effective masses

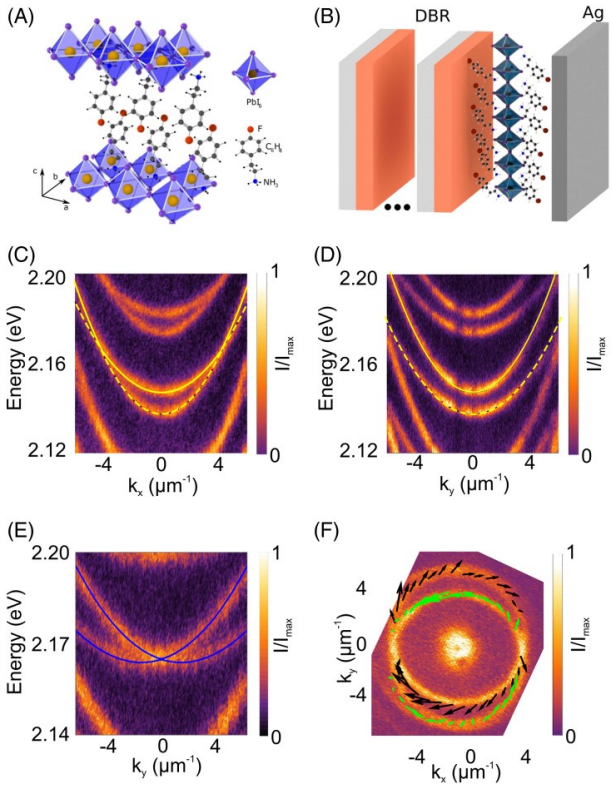

Fig. 1. Experimental implementation of a non-Abelian gauge field. A: Sketch of a PEAI-F 2*D* perovskite structure. B: Schematic representation of the microcavity sample. Perovskite flakes are embedded in an optical microcavity made by a distributed Bragg reflector (7 TiO_2/SiO_2 pairs) and a 80-nm-thick silver mirror. C, D: Experimental dispersions along k_x and k_y showing two diabolical points along k_x. E: Experimental dispersion along k_y for a fixed value of $k_x = 4.48\ \mu m^{-1}$ (crossing point) highlights the formation of a Rashba-type dispersion. Solid and dashed lines are the theoretical fits of the modes dispersion (parameters are given in the main text). F: Transmission map at the diabolical point energy together with the pseudo-spin orientation (black and green arrows) of the eigenstate obtained from polarization measurements. The monopolar pseudospin texture around the diabolical points is another signature of the Rashba SOC.

m_{TM}, m_{TE}. The perovskite excitons located at 2.39 eV are strongly coupled with the photonic modes of the cavity, forming exciton-polariton modes (polaritons) at room temperature [23] with a Rabi splitting of 208 meV. Thanks to the presence of the fluorine, the crystal symmetry of the perovskite determines a strong linear birefringence. Such birefringence, and all the effects we are describing, could be obtained for bare photonic modes, whereas strong coupling allows us to get the effect with a sizeable magnitude. The birefringence breaks the cylindrical symmetry of the TE and TM modes and lifts their degeneracy at k_x, $k_y = 0$. Figures 1C and 1D show the dispersion maps of the cavity transmission for wavevectors along the two perpendicular orientations k_x, k_y. Our microcavity is relatively thick ($\simeq 7\ \mu m$) and the quantized polarization doublets are close to each other, separated by about 50 meV. Within a polarization doublet, the behavior is radically different along the two wavevector orientations and can be understood by writing down an effective Hamiltonian in the parabolic approximation on the circular polarization basis [17]:

$$H_{\boldsymbol{k}} = \begin{pmatrix} E_0 + \frac{\hbar^2 k^2}{2m} & \beta_0 - \beta k^2 e^{-2i\varphi} \\ \beta_0 - \beta k^2 e^{2i\varphi} & E_0 + \frac{\hbar^2 k^2}{2m} \end{pmatrix}, \quad (2)$$

where $m = m_{\mathrm{TM}}\, m_{\mathrm{TE}}/(m_{\mathrm{TM}} + m_{\mathrm{TE}})$. $k = |\boldsymbol{k}| = \sqrt{k_x^2 + k_y^2}$ is the in-plane wavevector ($k_x = k\cos\varphi$, $k_y = k\sin\varphi$, φ is the propagation angle). β_0 is the optical birefringence. This effective Hamiltonian is expected to describe each of the polarization doublets with different parameter values (two of them are reported in Figs. 1C and 1D). By working with other polarisation doublets—for which the exciton–photon fractions are different—we can also scan over different values of these parameters. Along k_x, the X-polarized mode corresponds to the TM mode with the smaller mass. The two parabola cross at $k_x^0 = (\beta_0/\beta)^{1/2} = \pm 4.48\ \mu\mathrm{m}^{-1}$, as shown in Fig. 1C, giving rise to a diabolical point. Along k_y, ($\varphi = \pi/2$), the off-diagonal terms add up. It means that the lowest polarization mode at $k = 0$ (polarized along X) corresponds to the TE mode with the larger mass: the splitting increases with k_y (Fig. 1D). The fit of the experimental data with the effective Hamiltonian (2) yields $E_0 = 2.1415$ eV, $m = 2.4 \cdot 10^{-5} m_e$, $\beta = 2.5 \cdot 10^{-4}$ eV μm^2, and $\beta_0 = 10$ meV. m_e is the free electron mass.

Interestingly, around this diabolical point, the effective Hamiltonian can be rewritten [17,19] as a Rashba-like Hamiltonian [14]

$$\hat{H}_R = \frac{1}{2m}\hat{\boldsymbol{p}}^2 + \alpha\boldsymbol{\sigma}\cdot\hat{\boldsymbol{p}} = \frac{1}{2m}\left(\hat{\boldsymbol{p}} + m\alpha\boldsymbol{\sigma}\right)^2 - m\alpha^2\sigma^0, \qquad (3)$$

where $\boldsymbol{\sigma}$ is a vector of Pauli matrices. $p = \hbar q$ is the momentum, $q = k - k_y^0$. In addition, $\alpha = \sqrt{\beta_0\beta/2}$. The Rashba-like nature of this diabolical point is experimentally proven in Figs. 1E and 1F. Figure 1E shows the dispersion along k_y at $k_x = k_y^0$, which demonstrates a conical shape around the crossing point. Figure 1F shows the pseudospin distribution of the eigenstates at the energy of the crossing point. The pseudospin is deduced from the measured polarisation degree of the trasmission signal (see Methods and Supplement 1, Fig. S3). One can see that the pseudospin is pointing in opposite directions at each side of the crossing (black and green arrows), in agreement with the Rashba Hamiltonian picture. The visibility of the crossing point, given by $k_y^0 = (\beta_0/\beta)^{1/2}$, is considerably enhanced compared to GaAs-based microcavities [19] due to the large birefringence of the PEAI-F.

A general non-relativistic Hamiltonian of a massive matter field (quantum particle) minimally coupled with a non-Abelian gauge field determined by a vector potential A_μ^a reads:

$$H_{\mathrm{YM}} = \frac{1}{2m}\left(\hat{\boldsymbol{p}} - \eta\boldsymbol{A}^a\sigma^a\right)^2 + \eta A_t^a\sigma^a. \qquad (4)$$

It can be derived from the complete gauge-invariant Yang–Mills Lagrangian [1,2] (see Supplement 1, Section IV for details). Here, the coupling constant is $\eta = \hbar/2$ (the quantum of spin). We use upper number indices, a, 0–3 for Pauli matrices. Comparing this expression with Eq. (3), we see that only two components of the emergent vector potential are non-zero: $A_x^1 = -m\alpha/\eta$, $A_y^2 = -m\alpha/\eta$. The emergent vector potential is constant, but since the underlying symmetry group is SU(2) and not U(1) (which means that the gauge field is non-Abelian), a constant vector potential results in a non-zero field strength tensor with components given by $F_{\mu\nu}^a = \partial_\mu A_\nu^a - \partial_\nu A_\mu^a - \eta\varepsilon^{abc}A_\nu^b A_\mu^c$, where μ, ν span (t, x, y, z). The non-zero components read $F_{yx}^3 = -F_{xy}^3 = -m^2\alpha^2/\eta$ and they couple to the spatial degrees of freedom, as discussed below.

Similar to the Lorentz force, which is given by the product between the electric current and the field, the general form of the force provided by the non-Abelian field links a unified spin-current vector J and the field strength tensor F. The equations of motion for the velocity $\boldsymbol{v}$ and spin (color) $\boldsymbol{s}$ of a classical relativistic particle coupled to the non-Abelian field read:

$$m dv^\mu/d\tau = \boldsymbol{J}_\nu \cdot \boldsymbol{F}^{\mu\nu}, \quad d\boldsymbol{s}/d\tau = -\eta\boldsymbol{A}_\mu \times \boldsymbol{J}^\mu, \qquad (5)$$

where $\boldsymbol{J}_\nu = \boldsymbol{s}v_\nu$ is the spin current. These two equations are solved together to find the particle trajectory and spin dynamics [24].

In our case, the acceleration is given by $a_x = -4m\alpha^2 J_y^3/\hbar^2$ and $a_y = 4m\alpha^2 J_x^3/\hbar^2$, where J_x^3 and J_y^3 are the circular (spin-up/down) components of the polariton spin current propagating along x and y, respectively. The acceleration is therefore transverse, but it acts on the circular component of the spin current, instead of affecting the charge current as the Lorentz force. The magnitude of the force is given by $\alpha^2 = \beta_0\beta/2$, three orders of magnitude larger than in GaAs-based microcavities [19], thanks to the high anisotropy of the PEAI-F (high value of β_0). We stress that the effect of the effective magnetic non-Abelian field we consider here differs crucially from a simple spin-dependent Lorentz force appearing in the presence of Abelian gauge fields different for the two spin components [11,20,25], since the equations for the two spin components are decoupled. In particular, Ref. [20] corresponds to a special case with equal Rashba and Dresselhaus coupling constants. This case can still be mapped to an Abelian gauge field (different for different spins, which are uncoupled). A distinctive feature of a *non-Abelian* gauge field is a non-zero field tensor (and force), which can be present in spite of a constant vector potential. For equal Rashba and Dresselhaus constants, such field and force are absent [12].

To demonstrate experimentally this transverse acceleration, we use a unique specificity of cavity polaritons: the possibility to resonantly create a wave packet with a well-defined pseudospin, centered on a specific state in reciprocal space, and then to study its real space evolution. The first experiment we perform consists in exciting resonantly the vicinity of the Rashba diabolical point with a pulsed polarized laser, which in the language of Yang–Mills gauge theories corresponds to creating a color current. The energy of the laser is tuned to the diabolical point, while the wavevector is slightly detuned from it, providing a color (spin) current. The scheme of the experiment is shown in Fig. 2A. The blue, white and red arrows represent the sigma+, vertical and sigma- polarization states of the incident laser, respectively.

Figures 2B–2D show the spatial intensity distribution together with the center-of-mass trajectories for three excitation conditions: σ^+, vertical, and σ^- polarization, respectively ($s^3 = 1, 0, -1$ with $s^1 = 0, 1, 0$). The difference between the three cases is also clearly visible on the transverse profiles of the total intensity (Fig. 2H). In an ideal case, the center of mass trajectory and circular polarisation degree (charge vector) shown in Fig. 2I are expected to be reproduced theoretically (Fig. 2J) by the equations of motion (5) using parameters m, α, β, β_0 extracted from the experiments and given above. Red and blue colors in the figure correspond to the two s^3 spin components (σ^+ and σ^-) and are strongly correlated with the trajectories. The non-Abelian magnetic-like field acts on the spin currents, which exhibit lateral deviations depending on their spin and velocity. At the same time, the spin itself changes depending on the propagation direction. This gives rise to opposite oscillating trajectories for red (σ^+) and blue (σ^-) wave packets. Both effects are absent for spinless excitation (vertical polarization): the wave packet propagates along a straight line. The correlated

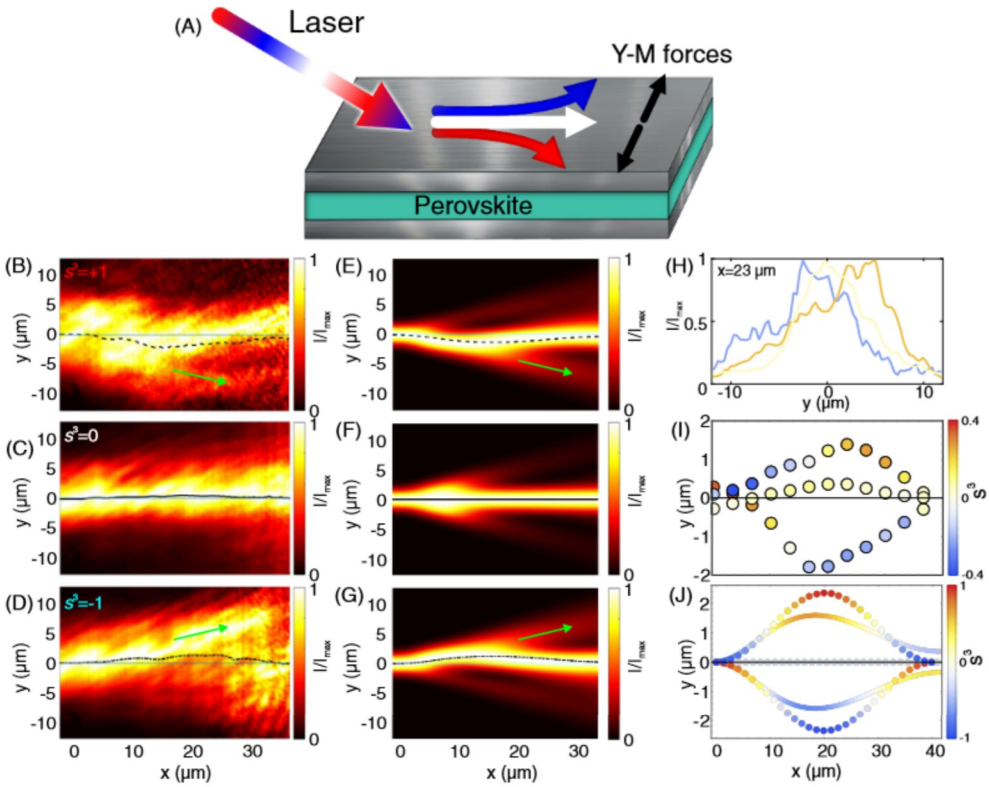

Fig. 2. Polariton propagation in a non-Abelian field. A: Scheme of the experiment. A polarized laser creates a flow that is deviated by the gauge field, depending on the sign of the spin current. Polarization of the excitation: left-circular ($s^3 = -1$), vertical ($s^1 = 1$, $s^3 = 0$), right-circular ($s^3 = 1$). B–D: Spatial images of the total emission intensity for the three spin excitation conditions. Log-scale false color map is used for all images. The dashed lines are the center of mass trajectories. B: $s^3 = +1$, the center of mass deviated downwards and then back. C: $s^3 = 0$, the center of mass has no deviation along the in-plane propagation. D: $s^3 = -1$, the center of mass deviated upwards and then back. E–G: Calculated spatial images of the total emission intensity based on Eq. (2) for three excitations ($s^3 = -1$, 0, 1). H: Transverse profiles of the total intensity at $x = 20$ μm (curve color corresponds to local s^3 of emission). I: Experimentally measured center of mass trajectories extracted from panels B–D and spin dynamics for three excitation conditions ($s^3 = -1$, 0, 1). Dot color corresponds to s^3. J: Classical simulations of propagation trajectories and spin for the same initial conditions ($s^3 = -1$, 0, 1). Dot color corresponds to s^3. Lines are extracted from the quantum simulations (E–G).

evolution of the wave packet position and its spin, described by the Eq. (5), is a specific feature of a non-Abelian gauge field: the spatial dynamics is controlled by the evolution of the vectorial charge, making an important difference with the spin-dependent Abelian fields [11,20], where the spin does not change over time. The scale of the effect is much larger than the typical deviation (the Hall angle) for the Hall effect [26] and of the same order as that of the spin Hall effect [27]. The deviation of the spin current from the straightforward trajectory is known as a manifestation of a "spin transverse force" in spintronics (and also in photonics [18]) since [28], while the configuration was understood to be a particular case of a non-Abelian Yang–Mills field only later [12].

In Figs. 2B and 2D, a secondary intensity peak appears around $x \approx 20$ μm (green arrows). As a result, the center of mass trajectory deviates from the straight trajectory. This is also visible in Fig. S4 of Supplement 1, showing waterfall plots of the transverse intensity at different x. The wave packet splitting is due to its finite size: for some components, the spin becomes aligned with the effective field and its precession stops, while the non-Abelian magnetic force becomes zero. This is confirmed by the full simulations based on the spinor Schrödinger equations with the Hamiltonian (2), shown in Figs. 2E–2G, where a second peak appears and propagates away from the center. The center of mass trajectory and spin extracted from the Schrödinger simulations are shown in Fig. 2J, where they are compared with the results of the classical equations (5). We conclude that this secondary peak is a real feature depending on the wave packet finite size and is not due to experimental imperfections, such as the disorder-induced scattering.

The second experiment consists of creating an energy potential in the plane of the cavity and launch the flow of spin-neutral particles (vertically polarized polaritons, $s^1 = 1$, $s^3 = 0$) against this defect, as shown in Fig. 3A. This type of experiment in the high density regime and with a standard microcavity dispersion allowed to demonstrate polariton superfluidity [29,30], the formation of oblique solitons [31], half-solitons [32], and of vortex anti-vortex pairs [33]. Here, we excite the flow with polarized light at the emergent diabolical point of the dispersion, in the linear, low density regime.

The polariton flow (black line, Fig. 3B) is upstream (left side of defect) and downstream (right side of defect). Upstream, the particle trajectory is strongly constrained by the defect potential and by the quantum pressure. The effect of the non-Abelian magnetic force is negligible compared to these two other contributions. However, the effects of the gauge field on the spin evolution, described by the second equation in (5), are not negligible. For downward propagation, the gained s^3 components, proportional

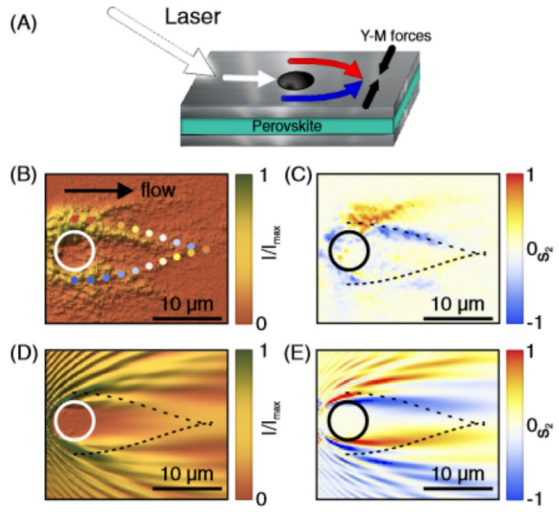

Fig. 3. Non-Abelian dynamics behind a defect potential. A: Scheme of the experiment. A linear-polarized laser creates a propagating flow, which hits a potential and splits into circular-polarized flows deviated by the non-Abelian magnetic field. The curve blue and red arrows schematically indicate the spatial deviation of the left- (s3=-1) and right- (s3=1) circular polarized flow, respectively. B: Experimental image of the total emission intensity (false color). Colored dots show the theoretical results (color corresponds to the s^3 spin projection, the scale is the same as on Fig. 3). The white circle shows the position of the potential defect. C: Experimental image of the difference between the diagonal polarization intensities (s^2). Dashed lines mark the theoretical trajectories. D, E: Calculated total intensity and s^2 based on Eq. (1).

to J_y^1, have opposite signs. Opposite spins are thus generated above and below the defect, as shown in the sketch Fig. 3A. In the region after the defect, the magnetic non-Abelian force becomes dominant, and the coupled equations (5) completely describe the particle trajectories and their spins. Due to the opposite spin (and therefore of the spin currents J_x^3) above and below the spatial defect (Figs. 3B and 3C), the transverse force in Eq. (5) is also opposite. This force brings the particles into the shadow of the defect. This convergent flow is clearly visible in Fig. 3B, showing experimental spatial image of the total particle density. The results of the simulations based on Eq. (5) corresponding to the wave packet trajectories are shown as points, whose color shows the s^3 spin projection. Figure 3C presents the difference between the s^2 components (chosen as the new spin basis), showing the best contrast due to the particular spin dynamics. Dashed lines show the calculated particle trajectories (same as in panel B). We also show the results of the full spinor Schrödinger simulations based on Eq. (2) in Figs. 3D and 3E. The agreement between the experiment and the classical and quantum simulations confirms that the density flows observed in total intensity in Fig. 3B originate from the non-Abelian coupled spin and spatial dynamics.

We would like to underline that these curved trajectories have nothing in common with the recently observed anomalous Hall drift [19] of accelerated polariton wave packets, which is induced by the non-zero Berry curvature of the polariton bands when time-reversal symmetry is broken. Anomalous Hall effect caused by an emergent Abelian magnetic field in the *reciprocal* space occurs during the adiabatic motion of a wave packet within a *single* band. On the opposite, the non-Abelian magnetic field in the present work acts in *real* space, and the oscillating trajectories in Figs. 2 and 3 are due to beatings between *two* coherently excited eigenstates, that is spin precession, described by the second equation in Eq. (5). We note that different types of oscillating or wiggling patterns, often called Zitterbewegung, are generally caused by beatings between two or more eigenstates. They are studied theoretically and experimentally in different photonic systems [34–36] including polaritons [37,38]. The advantage of our configuration is that the behavior of the beam can be described by Eq. (5), taking into account a non-Abelian gauge field, which is in general not possible for an arbitrary system exhibiting Zitterbewegung. These equations provide an analytical description of the system's behavior, giving expressions for the transverse acceleration as a function of the spin current.

3. CONCLUSION

Our work offers an experimental investigation of the spin-dependent particle trajectories in a non-Abelian gauge field obtained by using a 2D perovskite-based microcavity at room temperature. This physics is accessible thanks to the high anisotropy of the material that induces the formation of diabolical points in the polariton dispersion. Despite the stability issues and short propagation lengths imposed by the sample, we successfully measured the lateral deviation of the spin currents of a resonantly injected propagating polariton wave packet. The analogy with the Rashba-type SOC Hamiltonian in an engineered polariton system [13] offers an extremely straightforward platform for experimental studies which are hardly accessible in the field of particle physics, where complex interactions are often encountered.

Funding. Horizon 2020 Framework Programme (846353); Agence Nationale de la Recherche (ANR-16-CE30-0021, ANR-11-LABX-0014, ANR-16-IDEX-0001); Ministero dell'Istruzione, dell'Università e della Ricerca (B83B17000010001, 2017P9FJBS_001); Consiglio Nazionale delle Ricerche.

Acknowledgment. The authors acknowledge Paolo Cazzato for technical support, Iolena Tarantini for the metal evaporation, Sarah Porteboeuf-Houssais and Jean Orloff for useful discussions about quantum chromodynamics. We acknowledge the project TECNOMED-Tecnopolo di Nanotecnologia e Fotonica per la Medicina di Precisione" (Ministry of University and Scientific Research (MIUR) Decreto Direttoriale n. 3449 del 4/12/2017, CUP B83B17000010001), The project of the Ministry of University and Scientific Research (MIUR), PRIN 2017P9FJBS_001 Interacting Photons in Polariton Circuits-INPhoPOL. G.G. gratefully acknowledges the project PERSEO-PERrovskite-based Solar cells: towards high Efficiency and lOng-term stability (Bando PRIN 2015—Italian Ministry of University and Scientific Research (MIUR) Decreto Direttoriale 4 novembre 2015*n*.2488, project number 20155*LECAJ*).

Disclosures. The authors declare no conflicts of interest.

Data Availability. Data underlying the results presented in this paper are available in [39].

Supplemental document. See Supplement 1 for supporting content.

†These authors contributed equally to this work.

REFERENCES

1. C. N. Yang and R. L. Mills, "Conservation of isotopic spin and isotopic gauge invariance," Phys. Rev. **96**, 191–195 (1954).
2. L. H. Ryder, *Quantum Field Theory: Second Edition* (Cambridge University, 1996).
3. P. W. Higgs, "Broken symmetries and the masses of gauge bosons," Phys. Rev. Lett. **13**, 508–509 (1964).
4. C. Quigg, *Gauge Theories of the Strong, Weak, and Electromagnetic Interactions* (Addison-Wesley, 1997).

5. M. Aidelsburger, S. Nascimbene, and N. Goldman, "Artificial gauge fields in materials and engineered systems," C.R. Phys. **19**, 394–432 (2018).
6. M. V. Berry, "Quantal phase factors accompanying adiabatic changes," Proc. R. Soc. London A **392**, 45–57 (1984).
7. M. Z. Hasan and C. L. Kane, "Colloquium: Topological insulators," Rev. Mod. Phys. **82**, 3045–3067 (2010).
8. L. Lu, J. D. Joannopoulos, and M. Soljačić, "Topological photonics," Nat. Photonics **8**, 821 (2014).
9. T. Ozawa, H. M. Price, A. Amo, N. Goldman, M. Hafezi, L. Lu, M. C. Rechtsman, D. Schuster, J. Simon, O. Zilberberg, and I. Carusotto, "Topological photonics," Rev. Mod. Phys. **91**, 015006 (2019).
10. N. R. Cooper, J. Dalibard, and I. B. Spielman, "Topological bands for ultracold atoms," Rev. Mod. Phys. **91**, 015005 (2019).
11. F. Liu, T. Xu, S. Wang, Z. H. Hang, and J. Li, "Polarization beam splitting with gauge field metamaterials," Adv. Opt. Mater. **7**, 1801582 (2019).
12. P.-Q. Jin, Y.-Q. Li, and F.-C. Zhang, "Su(2)xu(1) unified theory for charge, orbit and spin currents," J. Phys. A **39**, 7115 (2006).
13. I. V. Tokatly, "Equilibrium spin currents: Non-abelian gauge invariance and color diamagnetism in condensed matter," Phys. Rev. Lett. **101**, 106601 (2008).
14. Y. A. Bychkov and É. I. Rashba, "Properties of a 2D electron gas with lifted spectral degeneracy," J. Exp. Theor. Phys. Lett. **39**, 78 (1984).
15. Y.-J. Lin, K. Jimenez-Garcia, and I. B. Spielman, "Spin–orbit-coupled Bose–Einstein condensates," Nature **471**, 83 (2011).
16. Z. Wu, L. Zhang, W. Sun, X.-T. Xu, B.-Z. Wang, S.-C. Ji, Y. Deng, S. Chen, X.-J. Liu, and J.-W. Pan, "Realization of two-dimensional spin-orbit coupling for Bose-Einstein condensates," Science **354**, 83–88 (2016).
17. H. Terças, H. Flayac, D. Solnyshkov, and G. Malpuech, "Non-abelian gauge fields in photonic cavities and photonic superfluids," Phys. Rev. Lett. **112**, 066402 (2014).
18. Y. Chen, R.-Y. Zhang, Z. Xiong, Z. Hong Hang, J. Li, J. Q. Shen, and C. T. Chan, "Non-abelian gauge field optics," Nat. Commun. **10**, 3125 (2019).
19. A. Gianfrate, O. Bleu, L. Dominici, V. Ardizzone, M. De Giorgi, D. Ballarini, G. Lerario, K. West, L. Pfeiffer, D. Solnyshkov, D. Sanvitto, and G. Malpuech, "Measurement of the quantum geometric tensor and of the anomalous Hall drift," Nature **578**, 381–385 (2020).
20. K. Rechcińska, M. Król, R. Mazur, P. Morawiak, R. Mirek, K. Łempicka, W. Bardyszewski, M. Matuszewski, P. Kula, W. Piecek, P. G. Lagoudakis, B. Pietka, and J. Szczytko, "Engineering spin-orbit synthetic Hamiltonians in liquid-crystal optical cavities," Science **366**, 727–730 (2019).
21. T. T. Wu and C. N. Yang, "Concept of nonintegrable phase factors and global formulation of gauge fields," Phys. Rev. D **12**, 3845–3857 (1975).
22. Y. Yang, C. Peng, D. Zhu, H. Buljan, J. D. Joannopoulos, B. Zhen, and M. Soljacic, "Synthesis and observation of non-abelian gauge fields in real space," Science **365**, 1021 (2019).
23. A. Fieramosca, L. De Marco, M. Passoni, L. Polimeno, A. Rizzo, B. L. Rosa, G. Cruciani, L. Dominici, M. De Giorgi, G. Gigli, L. C. Andreani, D. Gerace, D. Ballarini, and D. Sanvitto, "Tunable out-of-plane excitons in 2d single-crystal perovskites," ACS Photon. **5**, 4179–4185 (2018).
24. A. D. Boozer, "Classical Yang-Mills theory," Am. J. Phys **79**, 925–931 (2011).
25. M. C. Beeler, R. A. Williams, K. Jimenez-Garcia, L. J. LeBlanc, A. R. Perry, and I. B. Spielman, "The spin Hall effect in a quantum gas," Nature **498**, 201 (2013).
26. T. R. Chien, Z. Z. Wang, and N. P. Ong, "Effect of Zn impurities on the normal-state Hall angle in single-crystal yBa_2 Cu_{3-x} Zn_x $O_{7-\delta}$," Phys. Rev. Lett. **67**, 2088–2091 (1991).
27. Y. Wang, P. Deorani, X. Qiu, J. H. Kwon, and H. Yang, "Determination of intrinsic spin Hall angle in pt," Appl. Phys. Lett. **105**, 152412 (2014).
28. S.-Q. Shen, "Spin transverse force on spin current in an electric field," Phys. Rev. Lett. **95**, 187203 (2005).
29. A. Amo, J. Lefrere, S. Pigeon, C. Adrados, C. Ciuti, I. Carusotto, R. Houdre, E. Giacobino, and A. Bramati, "Superfluidity of polaritons in semiconductor microcavities," Nat. Phys. **5**, 805–810 (2009).
30. G. Lerario, A. Fieramosca, F. Barachati, D. Ballarini, K. S. Daskalakis, L. Dominici, M. De Giorgi, S. A. Maier, G. Gigli, S. Kéna-Cohen, and D. Sanvitto, "Room-temperature superfluidity in a polariton condensate," Nat. Phys. **13**, 837–841 (2017).
31. A. Amo, S. Pigeon, D. Sanvitto, V. G. Sala, R. Hivet, I. Carusotto, F. Pisanello, G. Leménager, R. Houdré, E. Giacobino, C. Ciuti, and A. Bramati, "Polariton superfluids reveal quantum hydrodynamic solitons," Science **332**, 1167–1170 (2011).
32. R. Hivet, H. Flayac, D. D. Solnyshkov, D. Tanese, T. Boulier, D. Andreoli, E. Giacobino, J. Bloch, A. Bramati, G. Malpuech, and A. Amo, "Half-solitons in a polariton quantum fluid behave like magnetic monopoles," Nat. Phys. **8**, 724–728 (2012).
33. L. Dominici, R. Carretero-Gonzalez, A. Gianfrate, J. Cuevaz-Maraver, A. S. Rodrigues, D. J. Frantzeskakis, G. Lerario, D. Ballarini, M. De Giorgi, G. Gigli, P. G. Kevredikis, and D. Sanvitto, "Interactions and scattering of quantum vortices in a polariton fluid," Nat. Commun. **9**, 1467 (2018).
34. F. Dreisow, M. Heinrich, R. Keil, A. Tünnermann, S. Nolte, S. Longhi, and A. Szameit, "Classical simulation of relativistic zitterbewegung in photonic lattices," Phys. Rev. Lett. **105**, 143902 (2010).
35. Q. Guo, W. Gao, J. Chen, Y. Liu, and S. Zhang, "Line degeneracy and strong spin-orbit coupling of light with bulk bianisotropic metamaterials," Phys. Rev. Lett. **115**, 067402 (2015).
36. R.-P. Guo, Q.-H. Guo, L.-T. Wu, J. Chen, and D. Fan, "Optical spin-sensitive zitterbewegung in bianisotropic metamaterials," Opt. Express **24**, 13788–13799 (2016).
37. E. S. Sedov, Y. G. Rubo, and A. V. Kavokin, "Zitterbewegung of exciton-polaritons," Phys. Rev. B **97**, 245312 (2018).
38. E. S. Sedov, I. E. Sedova, S. M. Arakelian, and A. V. Kavokin, "Magnetic control over the zitterbewegung of exciton–polaritons," New J. Phys. **22**, 083059 (2020).
39. D. D. Solnyshkov, "Raw data stored at the Open Science Framework website," Data file (2020), https://osf.io/3bewt/?view_only=1aab2f2d01d247df89c7eb6ab6b82523.